

Highlights

Optimal Sensor Placement and Estimator-Based Temperature Control for a Deep Drawing Process

Malte Wrobel, Thomas Meurer

- Model derivation and Finite Element approximation for a deep drawing tool with high geometric complexity.
- Experimental parameter identification.
- Comparison and evaluation of different model order reduction techniques.
- Optimal sensor placement, estimator design, and temperature control design based on the reduced order model.
- Experimental validation of the setup.

Optimal Sensor Placement and Estimator-Based Temperature Control for a Deep Drawing Process

Malte Wrobel^{a,*}, Thomas Meurer^a

^a*Digital Process Engineering Group, Institute for Mechanical Process Engineering and Mechanics, Karlsruhe Institute of Technology (KIT), Hertzstr. 16, Karlsruhe, 76187, Germany*

Abstract

Deep drawing is one of the most important forming processes for the forming of flat sheet blanks, where the formation of wrinkles and the appearance of cracks can be a problem, especially in areas of high geometric complexity. The local increase of the temperature in these critical areas can help to improve the formability of the material and thus reduce defects. The present paper aims at a targeted temperature control of the die of a deep-drawing mold. For this sensors are placed systematically to develop an estimator for the spatial-temporal temperature evolution to subsequently realize tracking control using the embedded actuation devices. A continuum representation of the temperature distribution in the die is derived and transferred to a high order finite element (FE) approximation to take the complex-shaped geometry of the tool into account. Parameter identification is performed based on measurement data to improve the accuracy of the FE approximation and model order reduction (MOR) techniques are applied to determine a sufficiently low order system representation. A mixed-integer optimization problem is formulated and solved making use of different formulations of the observability Gramian to determine the optimal sensor locations and a Kalman filter is designed as an estimator based on a reduced order model. Moreover, a linear-quadratic regulator with integral part combined with the Kalman filter is developed to react efficiently towards disturbances. Finally this theoretical framework is tested in a real experiment.

Keywords: Deep drawing, Finite Element method, Metal sheet forming, Model order reduction, Estimator design, Optimal control, Optimal sensor placement, Parameter identification, Partial differential equations, Software sensor, Temperature control, Linear quadratic regulator

1. Introduction

The production of increasingly complex structures has been a crucial requirement for the development of new products and a key contributor to the growth of a wide range of industrial sectors in recent decades. Metals, which are still the most widely used class of materials due to their outstanding mechanical properties, have entered new areas of application through a wide variety of manufacturing processes and, thanks to the latest technologies for component design, at competitive cost. Most of the metals are used in the industry with large lot productions, e.g. a statistical car consists of 90% components made by metal forming processes [1]. The focus for high-volume products, such as those in the automotive industry, is therefore on fast and cost-effective production with reproducible high quality, defined by design, surface quality, geometric accuracy, and hardness. These properties should usually also be achieved in a resource- and energy-saving manner [2]. The material, which is usually supplied as sheet metal,

undergoes a wide variety of forming and machining processes. One of the most important forming processes for shaping flat sheet blanks is the deep drawing process described in [3] and [4], where the sheet metal, also known as the blank, is placed on the die and a defined force is applied via a drawing punch. Additionally so-called blank holders are used to ensure an adequate fixation of the sheet metal and to prevent slippage.

During the deep drawing process wrinkles and cracks can occur especially in areas of high geometric complexity. To minimize the possibility of the occurrence of such quality-reducing defects the temperature of the die can be increased during the process to get a better formability of the metal [5]. For a cost-effective production it is reasonable to only increase the temperature locally in the critical areas. In order to realize this, a targeted intervention by built-in actuators is developed together with the estimation of the spatial-temporal evolution of the temperature in the die. The project ZF4558805RU8 funded by the German Zentrales Innovationsprogramm Mittelstand (ZIM) aims at the development of active thermal control in specialized deep drawing tools. For this, the experimental device illustrated by the CAD image in Fig. 1 is built and equipped suitably. It is of high geometric complex-

*Corresponding author

Email addresses: malte.wrobel@kit.edu (Malte Wrobel), thomas.meurer@kit.edu (Thomas Meurer)

ity to ensure transferability to other deep drawing tools as a benchmark. In six critical areas a locally increased temperature is desired. For each of these areas, insertion elements are designed as part of the die and provided with actuators. The computer-aided designed experimental die with these elements is depicted in Fig. 2. To obtain information about the temperature distribution in the die thermocouples are placed both in the insertion elements and in the rest of the die. Note that a thermal imaging camera is not used in this study as it requires placement close to the tool. Measuring the temperature during the holding time of the forming process is hardly possible and for the open tool the optical measuring angle is quite small.

First experiments with the experimental device have shown the benefit of a heated die. In Fig. 3 two parts of the formed sheet metal (1050 aluminium alloy with a thickness of 0.5 mm) are depicted without heating the die (left) and with the insertion elements heated open-loop to approximately $T = 150^\circ\text{C}$ at the critical areas (right). Obviously a reduction of wrinkles is achieved, however the number of cracks remains nearly the same. The used temperature was evaluated as the best choice for the reduction of the defects. An occurring problem is the temperature decrease in the die as consequence of the cold forming punch. These results clearly support the approach of an active thermally controlled forming tool to keep the temperature at a suitably determined level during multiple consecutive forming steps.

Accurate active thermal control requires a mathematical model describing the spatial-temporal temperature evolution, which is derived based on the heat equation. The finite element (FE) method described in [6] is then applied for spatial discretization due to the complex geometry. Based on this model a parameter identification problem is formulated to determine the unknown parameters. Different model order reduction (MOR) techniques (see, e.g., [7, 8]) are applied and compared to obtain a reduced order model (ROM) suitable for the control and the estimator design. For the latter an optimal sensor placement is addressed to improve the temperature estimation capabilities, combining mathematical model and local sensor

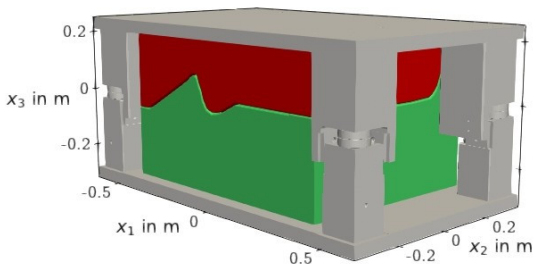


Figure 1: Computer-aided designed experimental deep drawing tool in total. The punch is visualized in red and the die in green.



Figure 2: Computer-aided designed experimental die (top view). Insertion element 1 is marked in yellow, 2 in magenta, 3 in light blue, 4 in dark blue, 5 in grey and 6 in dark red.

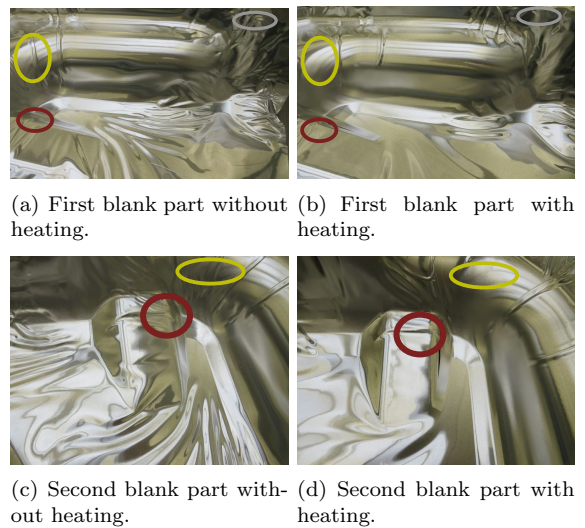


Figure 3: Two parts of a shaped blank with and without heating. The colored ellipsoids mark the positions of the insertion elements with respect to the used colors in Fig. 2.

information. In [9] different model order reduction (MOR) methods are compared minimizing the covariance matrix in order to find the optimal sensor positions, while in [10] and [11] the balanced model reduction is used. Maximizing the controllability Gramian is the aim of [12] and [8] to find the optimal actuator positions. In this work, the latter approach is transferred to address the sensor placement problem by maximizing the observability Gramian and some related measure as, e.g., proposed by [13]. This directly contributes to the system design as the determined locations are transferred to the experimental setup. This goes along with the incorporation of different model order reduction techniques (see, e.g., the surveys in [14, 7]) and a comparison with the full model. In particular a Kalman filter is implemented based on a ROM to evaluate the performance of the different sensor configurations. This Kalman filter is later tested in an experimental setup to validate sensor placement.

The transition between different temperature profiles in the die can be realized efficiently within a specified time in-

terval making use of a trajectory planning. Flatness based approaches are proposed by, e.g., [8, 15, 16] using e.g. a Gevrey function [17]. For our purposes a feedback control based on a ROM combined with the implemented Kalman filter is developed. Therefore a linear quadratic (LQ) regulator is used as in [18] for the optimal cooling of steel profiles and in [19] to handle stochastic parameter uncertainties. The regulator is extended by an integral part as proposed in [20] to reduce estimator errors efficiently. The whole setup is implemented at the experimental setup to validate the quality of the developed control loop.

The goal of the paper is to counteract the occurrence of wrinkles and cracks during a deep drawing process by a local temperature increase in critical areas of the die. This is realized by a targeted intervention by built-in actuators together with the estimation of the spatial-temporal evolution of the temperature in the die. The paper is organized as follows. Section 2 introduces the thermal model for the considered deep drawing tool and its FE approximation together with a parameter identification of the experimentally observed maximum power of the actuators and the heat transfer coefficient. The used MOR techniques are briefly described. Optimal sensor placement followed by the design of an estimator is addressed in Section 3. Section 4 introduces an estimator based controller design. Section 5 shows the results of the experiments performed to validate the theoretical developments. Some final remarks in Section 6 conclude the paper.

2. Modelling, Order Reduction and Parameter Identification

The heat equation is introduced to describe the spatial-temporal temperature evolution in the die. Based on this, a FE approximation is determined and the obtained model equations are reduced using different MOR techniques. A parameter identification based on experimental data is considered to determine the model parameters.

2.1. Continuum Representation

Mathematical modeling of the temperature distribution $T(x, t)$ in the die, whose spatial domain is denoted by Ω , leads to the heat equation

$$\rho c_p \partial_t T - \nabla \cdot (\lambda \nabla T) = 0, \quad (x, t) \in \Omega \times \mathbb{R}_0^+ \quad (1a)$$

with boundary and initial conditions

$$\mathbf{n} \cdot (\lambda \nabla T) = q_i u_i, \quad (x, t) \in \Gamma_i \times \mathbb{R}_0^+, \quad i \in I \quad (1b)$$

$$\mathbf{n} \cdot (\lambda \nabla T) = h(T_\infty - T), \quad (x, t) \in \Gamma_a \times \mathbb{R}_0^+ \quad (1c)$$

$$T = T_0, \quad x \in \Omega, \quad t = 0. \quad (1d)$$

Herein, $\rho = 7850 \text{ kg m}^{-3}$, $c_p = 460 \text{ J kg}^{-1} \text{ K}^{-1}$ and $\lambda = 34.5 \text{ J s}^{-1} \text{ m}^{-1} \text{ K}^{-1}$ denote density, specific heat capacity, and thermal conductivity of the material, the tool steel 1.2312 (40CrMnMoS8-6). Note that these parameters may

vary with $x = (x_1, x_2, x_3)$ to represent inhomogeneous or composite material. For reasons of simplicity they are chosen to be constant during the considered heating process. This is valid as the specific heat capacity of the steel is constant in the temperature range considered here. The boundary $\partial\Omega$ of the domain Ω is subdivided into $m = 6$ actuated subsets Γ_i , $i \in I = \{1, \dots, m\}$, where the external heating power $q_i u_i$, with maximal power q_i and the degree of actuation $u_i \in [0, 1]$ is applied, and the remaining surface Γ_a , which is in contact with the ambient air at uniform temperature T_∞ . Convective heat transfer between steel and air is described by the parameter h with SI unit $\text{W m}^{-2} \text{ K}^{-1}$. Radiative heat transfer is neglected as its contribution is much smaller compared to convective heat transfer in the experimental temperature range. The surface normal is denoted as \mathbf{n} . The actuators are not part of the domain Ω .

2.2. Meshing and FE Approximation

To take into account the complex geometry of the tool for control, the FE method is applied to (1). Based on the CAD construction of the tool shown in Fig. 1, the mesh of the die illustrated in Fig. 4 was generated using *Coreform Cubit 2020.2*. Critical areas involving curvatures at low radii can be clearly identified due to the comparatively tighter local mesh.

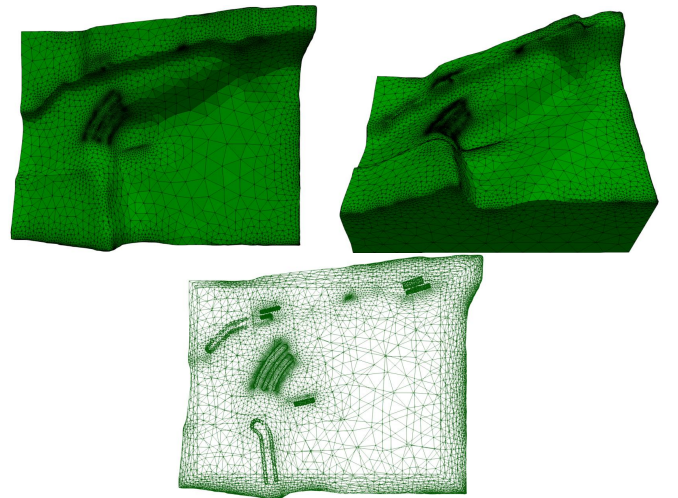


Figure 4: Meshed die, top view (left above) and view of the back side from Fig. 1 (right above) and wireframe view (below).

The FE approximation is evaluated using the software library *Firedrake* [21] in Python and leads to the finite-dimensional approximation in terms of the system of ordinary differential equations (ODEs)

$$E \dot{\mathbf{T}} = \mathbf{A} \mathbf{T} + \mathbf{B} \mathbf{u}, \quad t > 0, \quad \mathbf{T}(0) = \mathbf{T}^0. \quad (2)$$

in the nodal temperatures summarized in the vector $\mathbf{T}(t) \in \mathbb{R}^n$ with $n = 42819$. The elements of the thermal damping matrix $E \in \mathbb{R}^{n \times n}$, the thermal stiffness matrix $A \in \mathbb{R}^{n \times n}$,

and the input matrix $B = [\mathbf{b}_1, \mathbf{b}_2, \dots, \mathbf{b}_m] \in \mathbb{R}^{n \times m}$ are obtained from the variational form of (1). Herein, the test function $v \in V$ and the trial function $\phi \in V$, with V being a suitable function space for the solution of \mathbf{T} , are used, as described in [6]. The ambient temperature T_∞ is assumed constant, so the mapping $T(x, t) \mapsto T(x, t) - T_\infty$ or respectively

$$\mathbf{T}(t) \mapsto \mathbf{T}(t) - T_\infty \mathbf{1} \quad (3)$$

with $\mathbf{1} \in \mathbb{R}^n$ composed of only ones is introduced for the subsequent analysis and design. The input vector reads $\mathbf{u}(t) = [u_1(t), u_2(t), \dots, u_m(t)]^T$ with $u_i(t) \in [0, 1]$, $i = 1, \dots, m$ entering the system via the input vectors \mathbf{b}_i . This represents the heating elements with maximal power q_i for $u_i = 1$ defined in (1b). The output matrix $C \in \mathbb{R}^{p \times n}$ extracts the local temperatures at to be determined measurement locations inside and on the die, i.e.,

$$\mathbf{y} = C\mathbf{T}, \quad t \geq 0 \quad (4)$$

with $\mathbf{y}(t) \in \mathbb{R}^p$. In particular, p sensors are placed using the optimization setup addressed in Section 3.

2.3. Model Order Reduction

The large number of $n = 42819$ nodes leads to a computationally intensive calculation for simulation, one time step takes 1.2462 s, and makes the model unusable for control and estimator design purposes, which is discussed in Section 3 and Section 4. To cope with this difficulty a reduced order model (ROM) of significantly lower dimension $r \ll n$ is determined, which approximates the dynamics of the full order system with sufficient accuracy. Due to the model availability in terms of (2) and (4) projection-based MOR is considered. Following [7] the unknown state variables in a basis of reduced dimension are approximated and the governing equations are projected onto a suitably defined subspace of small dimension. The projection matrices $V \in \mathbb{R}^{n \times r}$ and $W \in \mathbb{R}^{n \times r}$ are used, where $\mathcal{V} = \text{range}(V)$ is an r -dimensional test subspace and $\mathcal{W} = \text{range}(W)$ an associated trial subspace. Approximating the full state $\mathbf{T}(t)$ evolving in the r -dimensional subspace \mathcal{V} in terms of $\mathbf{T}_r(t) \in \mathbb{R}^r$,

$$\mathbf{T} = V\mathbf{T}_r \quad (5)$$

is written. Taking into account the Petrov-Galerkin condition [7]

$$W^T (EV\dot{\mathbf{T}}_r - AV\mathbf{T}_r - B\mathbf{u}) = 0,$$

the substitution of (5) into (2), (4) yields

$$E_r \dot{\mathbf{T}}_r = A_r \mathbf{T}_r + B_r \mathbf{u}, \quad t > 0, \quad \mathbf{T}_r(0) = \mathbf{T}_r^0 \quad (6a)$$

$$\mathbf{y} = C_r \mathbf{T}_r. \quad (6b)$$

Herein, the reduced order matrices $E_r \in \mathbb{R}^{r \times r}$, $A_r \in \mathbb{R}^{r \times r}$, $B_r \in \mathbb{R}^{r \times m}$ and $C_r \in \mathbb{R}^{p \times r}$ are determined as

$$E_r = W^T E V, \quad A_r = W^T A V, \quad B_r = W^T B, \quad C_r = C V.$$

The calculation time of one time step reduces significantly to 0.0147 s for an exemplary reduction order $r = 95$. Subsequently, three different MOR techniques based on this projection are evaluated.

2.3.1. Balanced truncation

The controllability and observability Gramians depend on the respective choice of the coordinate system and will transform under a change of coordinates. A transformation with respect to the controllability and observability is called balanced, if the gramians W_c and W_o go together to $W_{c,r} = W_{o,r}$ becoming equal and diagonal [22].

Given (2), (4) and the fact that the spectrum of A is contained in the open left half plane, i.e., $\sigma(A) \subset \mathbb{C}_0^-$, the controllability and observability Gramians W_c and W_o can be calculated via the generalized Lyapunov equations

$$AW_c E^T + E W_c A^T + B B^T = 0, \quad (7a)$$

$$A^T W_o E + E^T W_o A + C^T C = 0. \quad (7b)$$

To solve these efficiently the low-rank alternating-direction implicit (ADI) method presented in, e.g., [23] is applied. Using the Cholesky decompositions $W_c = W_{c,C} W_{c,C}^T$, $W_o = W_{o,C} W_{o,C}^T$ and the singular value decomposition (SVD)

$$W_{c,C}^T W_{o,C} = [U_1 \quad U_2] \begin{bmatrix} \Sigma_1 & 0 \\ 0 & \Sigma_2 \end{bmatrix} \begin{bmatrix} V_1^T \\ V_2^T \end{bmatrix}$$

leads to the balancing transformations

$$W = W_{o,C} V_1 \Sigma_1^{-\frac{1}{2}}, \quad V = W_{c,C} U_1 \Sigma_1^{-\frac{1}{2}}.$$

For balanced truncation (BT) these matrices are used to evaluate (6). Herein, the MESS toolbox [24] in MATLAB is used for numerical evaluation.

2.3.2. Iterative rational Krylov algorithm

Moment matching (MM) methods in general aim at the construction of a lower degree rational transfer function $G_r(s)$ that matches the transfer function $G(s)$ of the full order system and its derivatives at certain points $s_k \in \mathbb{C}$ in the complex domain. The iterative rational Krylov algorithm (IRKA) is an MM method using an \mathcal{H}_2 -optimal shift set to determine W and V iteratively [25]. For the considered application the IRKA is solved using the sssMOR toolbox [26] in MATLAB.

2.3.3. Proper orthogonal decomposition

The proper orthogonal decomposition (POD) operates with a snapshot matrix to construct the transformation matrices [27]. Snapshots are computed by numerically solving the system (2), (4) subject to appropriate excitation signals \mathbf{u} . The SVD of the snapshot matrix leads to the transformation matrices V and W .

2.4. Parameter Identification

Heating elements are installed in order to locally increase the temperature in the die. These are placed in the $m = 6$ insertion elements $I = \{1, \dots, 6\}$ which are fully integrated in the die and consist of the same tool steel 1.2312 (40CrMnMoS8-6). The dimensions of the heaters, their maximum heating power and the type are listed in Table 1. Elements $i \in \{1, 2, 3, 6\}$ are equipped with one heater, elements $i \in \{4, 5\}$ with two heaters controlled in parallel. A sensor is installed in each of the elements. Due to non-ideal assembly and imperfections in installation the transferred and experimentally observed heating power does not directly correspond to the nominal values listed in Table 1. To address this and to cover the accumulated effects of the assembly and installation a parameter identification procedure is developed.

Together with the parameters of the actuators, the heat transfer coefficient of (1c) is addressed in this identification setup, as it is not exactly defined by the used material and therefore not known. For parameter identification, the insertion elements are separate components detached from the die. They are fully surrounded by the ambient air at uniform temperature T_∞ . A mathematical model for describing the temperature distribution over the respective domains is derived for all six insertion elements. The continuum representations are derived in the same way as in (1). To discretize the equations again the FE method is used. The meshes generated using *Coreform Cubit 2020.2* are illustrated in Fig. 5. As before the FE model is determined using the software library *Firedrake* [21] to obtain the set of ODEs

$$E_i \dot{\mathbf{T}}_i = A_i \mathbf{T}_i + B_i \mathbf{u}_i, \quad t > 0, \quad \mathbf{T}_i(0) = \mathbf{T}_i^0, \quad (8a)$$

$$y_i = \mathbf{c}_i^T \mathbf{T}_i, \quad t \geq 0. \quad (8b)$$

with

$$A_i = A_{\lambda,i} + hA_{h,i},$$

$$\mathbf{u}_i(t) = p\eta_i \left(1 - e^{-\frac{t}{\tau_i}}\right) \begin{cases} 1, & i \in \{1, 2, 3, 6\}. \\ \begin{bmatrix} 1 \\ 1 \end{bmatrix}, & i \in \{4, 5\}. \end{cases} \quad (8c)$$

The nodal temperatures are summarized in the vectors $\mathbf{T}_i(t) \in \mathbb{R}^{n_i}$ for $n_i, i = 1, \dots, m$. The elements of the

Table 1: Properties of the heating elements in the six insertion elements.

El. $i \in I$	Measures in mm	Power in W	Heater type
1	$\text{Ø}4 \times 930$	1200	Coil
2	$\text{Ø}8.5 \times 468$	1050	Tubular
3	$\text{Ø}8.5 \times 397$	900	Tubular
4	$\text{Ø}12.5 \times 65$	500	Cartridge
	$\text{Ø}12.5 \times 35$	300	Cartridge
5	$\text{Ø}20 \times 50$	600	Cartridge
	$\text{Ø}12.5 \times 70$	550	Cartridge
6	$\text{Ø}16 \times 60$	400	Cartridge

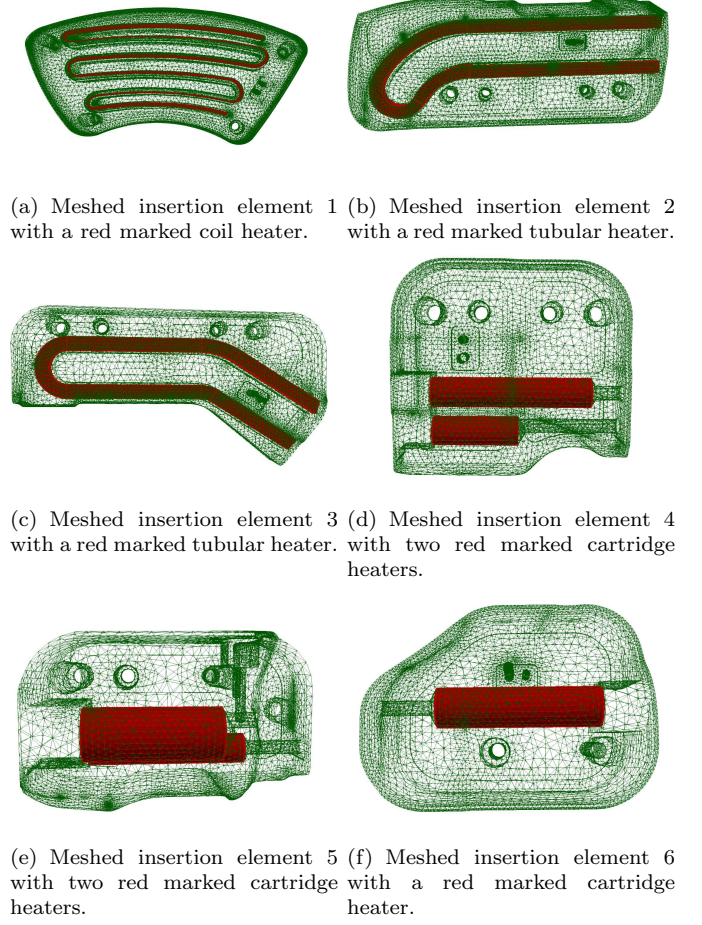


Figure 5: Meshes of the six insertion elements.

thermal damping matrices $E_i \in \mathbb{R}^{n_i \times n_i}$, the input matrices $B_i \in \mathbb{R}^{n_i \times 1}$ for $i \in \{1, 2, 3, 6\}$ and $B_i \in \mathbb{R}^{n_i \times 2}$ for $i \in \{4, 5\}$ and the thermal stiffness matrices $A_i \in \mathbb{R}^{n_i \times n_i}$ are obtained from the variational form of the continuum representation. Herein, $A_{\lambda,i}$ denotes the part of A_i resulting from (1a) of the heat equation and $A_{h,i}$ the part from (1c). This splitting enables the parameter identification of the heat transfer coefficient h . The output vectors $\mathbf{c}_i^T \in \mathbb{R}^{1 \times n_i}$ are used to project the nodal temperature to the measured outputs y_i . In the equations p is the degree of actuation and η_i can be interpreted as efficiency factors. The variables τ_i describe the delayed start-up of the actuators following a PT_1 behavior. The measured sensor values \tilde{y}_i are collected for all six insertion elements in two different scenarios resulting in two data sets $\{\tilde{y}_{p_1,i}\}_{i=1}^6$ and $\{\tilde{y}_{p_2,i}\}_{i=1}^6$. These differ in the used degree of actuation with

$$p_1 = \begin{cases} 0.1, & t \leq t_{1,i} \\ 0, & t > t_{1,i}. \end{cases}, \quad p_2 = \begin{cases} 1, & t \leq t_{2,i} \\ 0, & t > t_{2,i} \end{cases},$$

where $t_{1,i}$ and $t_{2,i}$ denote the points in time at which the degrees of actuation become zero to avoid extremely high

temperatures. During the experiments, the insertion elements were detached from the die. Making use of (8a) numerical solutions are determined for each insertion element for both actuation scenarios in each iteration of the optimization problem

$$\min_{h, \boldsymbol{\eta}, \boldsymbol{\tau}} J = \sum_{i=1}^m \|\tilde{y}_{p_1, i} - y_{p_1, i}\|_1 + \sum_{i=1}^m \|\tilde{y}_{p_2, i} - y_{p_2, i}\|_1,$$

where $y_{p_1, i}$ and $y_{p_2, i}$ refer to the simulated outputs, h is the to be determined heat transfer coefficient, and $\boldsymbol{\eta} = [\eta_1, \dots, \eta_6]^T$, $\boldsymbol{\tau} = [\tau_1, \dots, \tau_6]^T$ are the parameters in (8c).

The optimization problem results in $h = 6.6768 \text{ W m}^{-2} \text{ K}^{-1}$ and the values in Table 2. The optimization objective $J = 2321.5 \text{ K}$, which is equivalent to a temperature difference of $T_{\text{diff}} = 2321.5 \text{ K} / n_{\Delta t} \approx 0.9625 \text{ K}$ between optimized simulation and experimental data, is sufficiently small. Here, the total number of time steps in all data sets is $n_{\Delta t} = 2412$. Literature values for the heat transfer coefficient h between steel and air are in the range of $h = 5 \text{ W m}^{-2} \text{ K}^{-1}$ and $h = 30 \text{ W m}^{-2} \text{ K}^{-1}$ [28], which fit with the determined value. The results for the efficiency factors $\boldsymbol{\eta}$ are also plausible. As expected, they are smaller than, but close to 1 and state that the actuators have maximum heating powers of 78.36 % to 95.61 % of the data sheet values. The optimized values of the delay variables $\boldsymbol{\tau}$ result in transient responses between 9.9137 s and 40.4569 s, with the maximum value for the coil heater.

Table 2: Optimized values of the heating elements.

No. i	η_i	τ_i
1	0.9409	40.4569
2	0.8738	16.7488
3	0.8824	27.0662
4	0.9561	9.9137
5	0.7836	9.9217
6	0.9063	31.5385

Fig. 6 depicts the temporal evolution of the temperature in the two scenarios. The dashed lines represent the experimental data, while the continuous lines refer to the simulations results using (8a) with the determined parameters. The results clearly confirm that the dynamics of the insertion elements is rather accurately represented. Differences arise primarily for the fourth insertion element in the scenario p_2 , where temperatures above 200°C are induced. These may lead to simulation problems as the influence of the neglected effect of radiative heat transfer becomes more important.

3. Optimal Sensor Placement

To determine the most reasonable sensor positions in the die to gain insight into the process dynamics and to set up an estimator strategy an optimization-based approach is

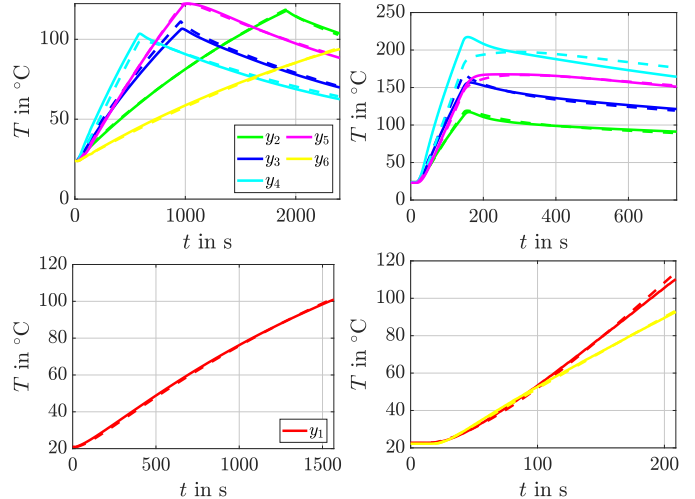


Figure 6: Simulations (continuous lines) and experimental data (dashed lines) of the six insertion elements in the scenarios with $p = p_1$ (left) and $p = p_2$ (right).

considered to place sensors. As the insertion elements are equipped with separate sensors a model of the die without these elements is used for optimization. This model is described in detail in [29]. The mesh is visualised in Fig. 7.

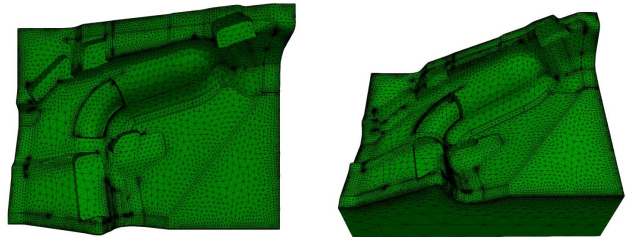


Figure 7: Meshed die, top view (left) and view of the back side from Fig. 1 (right).

3.1. Segmentation

For sensor placement the model geometry is divided into segments illustrated in Fig. 8. Segments in this context represent possible sensor positions used as decision variables in the optimal sensor placement problem introduced subsequently. The segments are created by dividing the x_1 -, x_2 - and x_3 -axes into 8, 7 and 4 elements, respectively. Since the surface in x_3 -direction varies in height in total $p = 166$ segments are considered with some not fully occupied by the tool volume.

The output equation for the segmentation is defined as

$$\mathbf{y}_{\text{seg}} = C_{\text{seg}} \mathbf{T}, \quad t \geq 0 \quad (9)$$

amending the finite-dimensional approximation (2). The vector $\mathbf{y}_{\text{seg}}(t) \in \mathbb{R}^p$ is composed of the temperatures averaged over each possible segment. Therefore the nonzero

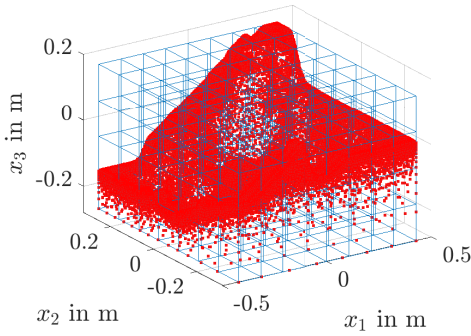


Figure 8: Nodes (red dots) and segments (cuboids) of the die.

elements of the sparse output matrix $C_{\text{seg}} \in \mathbb{R}^{p \times n}$ are defined as q^{-1} , with q being the number of nodes in the specific segment.

3.2. Optimization Problem

To quantify the level of observability of a particular sensor configuration the observability Gramian W_o is used, which contains the observable subspace of a system [22]. This matrix describes to which extent the system dynamics can be reconstructed by the placed sensors. The observability Gramian W_o can be computed by means of the generalized Lyapunov equation (7b) using C_{seg} as output matrix. The Gramian W_o depends on C_{seg} and thus on the placed sensors. Following $W_o(\boldsymbol{\chi})$ with the binary vector $\boldsymbol{\chi} \in \{0, 1\}^p$ is used representing a possible sensor configuration and $\chi_i = 1$ denoting a chosen segment. This method enables the possibility to define non-feasible segments.

3.2.1. MAX-DET optimization.

By making use of the results of [12] for the dual problem of optimal actuator placement the maximization of the determinant of W_o is considered as the maximum represents the volume of the observable subspace. This leads to

$$\max_{\boldsymbol{\chi}} \det(W_o(\boldsymbol{\chi})).$$

The observability Gramian $W_{o,i}$ is set up for each segment so that due to linearity

$$W_o(\boldsymbol{\chi}) = \sum_{i=1}^p \chi_i W_{o,i}$$

with the decision variables $\chi_i \in \{0, 1\}$, $i = 1, \dots, p$. To accelerate the calculation, an SVD is performed, i.e., $W_o = USV^T$, and only the s largest singular values $U_{1:s}$ are considered in the reduced Gramian $W_{o,red} = U_{1:s} W_o U_{1:s}^T$, where the first s columns of U are used to reduce the size of W_o from $\mathbb{R}^{n \times n}$ to $\mathbb{R}^{s \times s}$. This extracts the most relevant

information contained in the s largest singular values and yields the reduced optimization problem

$$\max_{\boldsymbol{\chi}} \det \left(\sum_{i=1}^p \chi_i U_{1:s} W_{o,i} U_{1:s}^T \right).$$

The maximization problem can be recast into a minimization problem by considering the inverse matrix and making use of the logarithm for better scaling. This results in the mixed-integer optimization problem

$$\min_{\boldsymbol{\chi}} \log \det \left(\sum_{i=1}^p \chi_i U_{1:s} W_{o,i} U_{1:s}^T \right)^{-1} \quad (10a)$$

$$\text{s.t.} \quad \sum_{i=1}^p \chi_i \leq p_{\text{max}}, \quad \chi_i \in \{0, 1\}, \quad (10b)$$

where p_{max} is the maximal number of sensors to be embedded into the die.

3.2.2. Alternative measures.

Following, e.g., [13] measures other than the MAX-DET optimization seem reasonable. This includes $\max(-\text{trace } W_o^{-1})$, which is proportional to the energy needed on average to observe the systems' states. Taking into account the previous exposition the resulting minimization problem reads

$$\min_{\boldsymbol{\chi}} \text{trace} \left(\sum_{i=1}^p \chi_i U_{1:s} W_{o,i} U_{1:s}^T \right)^{-1} \quad \text{s.t.} \quad (10b). \quad (11)$$

The measure $\max \text{trace } W_o$ is inversely related to the average energy of the system and calculates the average observability in all directions. This implies

$$\min_{\boldsymbol{\chi}} -\text{trace} \left(\sum_{i=1}^p \chi_i U_{1:s} W_{o,i} U_{1:s}^T \right) \quad \text{s.t.} \quad (10b). \quad (12)$$

To maximize the dimension of the observable subspace the rank of the Gramian can be maximized so that

$$\min_{\boldsymbol{\chi}} -\text{rank} \left(\sum_{i=1}^p \chi_i U_{1:s} W_{o,i} U_{1:s}^T \right) \quad \text{s.t.} \quad (10b). \quad (13)$$

It might also be useful to maximize the smallest eigenvalue $\lambda_{\min}(W_o)$ of the observability Gramian. This measures the amount of energy, which is needed to move the system into the direction that is most difficult to observe and implies

$$\min_{\boldsymbol{\chi}} -\lambda_{\min} \left(\sum_{i=1}^p \chi_i U_{1:s} W_{o,i} U_{1:s}^T \right) \quad \text{s.t.} \quad (10b). \quad (14)$$

3.2.3. Optimization using ROMs.

Solving the Lyapunov equation to obtain the observability Gramian W_o requires high computational power. Another intuitive way to calculate a reduced Gramian is

solving the Lyapunov equation (7b) for the ROM (6). This allows to transfer any of the optimization problems (10) to (14) by replacing W_o with the resulting ROM-based Gramian $W_{o,r}$. Since the sensor-dependent output matrix C , which has to be determined is not available, C_{seg} is used to create the ROM. Aiming, e.g., at the maximization of the smallest eigenvalue as in (14) this results in

$$\min_{\mathbf{x}} -\lambda_{\min} \left(\sum_{i=1}^p \chi_i U_{1:s} W_{o,r,i} U_{1:s}^T \right) \text{ s.t. (10b)}. \quad (15)$$

Subsequently, the distinction is made between the reduced observability Gramian $W_{o,r}$ computed using BT ($W_{o,\text{BT}}$), IRKA ($W_{o,\text{IRKA}}$), and POD ($W_{o,\text{POD}}$).

3.3. Optimal Sensor Configuration

Depending on the different measures (10) to (15) and observability Gramians the respective optimal sensor configurations are determined. For the numerical evaluations $s = 10$ is chosen so that the 10 largest singular values of the observability Gramian $W_{o,i}$ are used to represent the most relevant part of the dynamics.

3.3.1. Comparison of measures

The first optimizations are set up with the full model and $p_{\text{max}} = 8$. The optimality measure is varied to compare (10) to (14). For the solution of the mixed-integer optimization problems the Genetic Algorithm from the Global Optimization Toolbox of MATLAB is used as it can solve smooth and nonsmooth optimization problems including integer constraints. Fig. 9 shows the resulting sensor placement in the die, where the nodes inside the respective segments are marked red. Most of the chosen segments are distributed on the surface of the deep drawing tool. Covered segments include the area with highest x_3 -value, the center and the lower part in negative x_1 -direction. The flat area with positive x_1 - and negative x_2 -value is neglected in most cases. Maximizing the rank of W_o differs significantly. In this case many segments are inside the tool.

Remark 1 (Estimator design). To compare the performance of these sensor configurations an estimator is set up using the ROM (6) obtained from balanced truncation. There is a different ROM for each configuration, because the ROM depends on the output matrix C , which is set up by placing imaginary sensors at nodes near the center of the selected segments. For this purpose, a Kalman filter is used

$$E_r \dot{\hat{\mathbf{T}}}_r = A_r \hat{\mathbf{T}}_r + B_r \mathbf{u} + L (\mathbf{y} - \hat{\mathbf{y}}), \quad t > 0 \quad (16a)$$

$$\hat{\mathbf{T}}_r(0) = \hat{\mathbf{T}}^0 \quad (16b)$$

$$\hat{\mathbf{y}} = C_r \hat{\mathbf{T}}_r, \quad t \geq 0. \quad (16c)$$

minimizing the variance of the estimation error $\tilde{\mathbf{T}}_r(t) = \mathbf{T}_r(t) - \hat{\mathbf{T}}_r(t)$ under the assumption of zero mean Gaussian

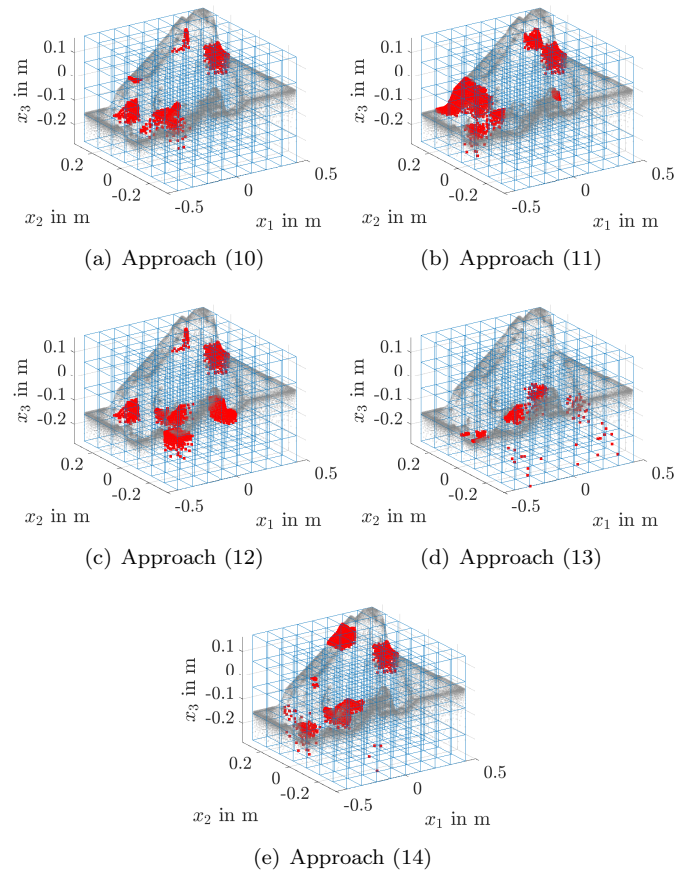


Figure 9: Selected sensor segments for the different optimization routines based on the full model.

process and measurement noise with covariances Q and R [30]. The static estimator gain matrix from (16) follows as $L = PC_r^T R^{-1}$ with the covariance matrix P obtained from solving the algebraic Riccati equation

$$0 = E_r P A_r^T + A_r P E_r^T - E_r P C_r^T R^{-1} C_r P E_r^T + Q.$$

This equation is not solvable for the full order model with a computer equipped with 16 GB RAM, which justifies the usage of the ROM. In the evaluations an appropriate input \mathbf{u} is chosen.

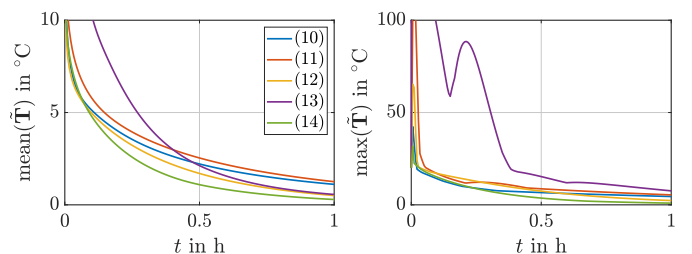


Figure 10: Comparison of the resulting estimation error for the sensor locations of Fig. 9.

Fig. 10 shows the estimation errors from the different sensor configurations. To guarantee comparability

Table 3: Estimation error analysis for Fig. 10.

Approach	$\text{mean}(\tilde{\mathbf{T}}(t))$	$\text{max}(\tilde{\mathbf{T}}(t))$	$\lambda_{\min}(W_o)$
(10)	0.7960	2.6708	1.2282e-05
(11)	0.8647	3.4461	7.8567e-06
(12)	0.5232	2.0963	1.1628e-07
(13)	0.8563	10.0819	1.1645e-10
(14)	0.4226	1.2924	7.1687e-05

the matrices Q and R are identity matrices for all configurations. The errors from the full model $\tilde{\mathbf{T}} = V\tilde{\mathbf{T}}_r$ are compared. The average error considering all nodes' $\text{mean}(\tilde{\mathbf{T}}(t)) = \sum_{i=1}^n \tilde{T}_i(t)/n$ is shown on the left and the maximum error of all nodes $\text{max}(\tilde{\mathbf{T}}(t))$ is shown on the right. Table 3 summarizes average estimation errors over a five hour time interval. Maximizing the rank of W_o in (13) gives poor results. The SVD reduced observability Gramian matrices has full rank in many cases, so this sensor configuration is nearly random. Maximizing the minimal eigenvalue of W_o using (14) emerges as the best sensor configuration. This measure is therefore given special consideration for comparison with the respective ROMs. Table 3 also shows the value of $\lambda_{\min}(W_o)$. This measure tends to evaluate sensor placement reasonably. Thus, (13) providing the worst observation result also implies the smallest value of $\lambda_{\min}(W_o)$.

3.3.2. Comparison of ROMs

Secondly, the discussed ROMs are used for optimal sensor placement by making use of the measure (15) and $p_{\max} = 8$. The arising mixed-integer optimization problems are solved as before. Fig. 11 summarizes the resulting sensor locations based on the computation with the full order model (here (14) is applied) and ROMs based on BT, IRKA and POD. In comparison to the sensor placement based on the full order model, the result obtained using the IRKA-ROM shows some tendency to locate sensors in the part with negative x_1 -coordinate. The result of the BT-ROM configuration resembles the sensor segments of the full order model. The segments of the POD-ROM configuration are fewer represented in the middle of the tool. The performance of these sensor configurations is compared similarly to the previous case by setting up a respective estimator. As before the matrices Q and R are chosen as identity matrices for all configurations.

Table 4: Estimation error analysis for Fig. 12.

Approach	$\text{mean}(\tilde{\mathbf{T}}(t))$	$\text{max}(\tilde{\mathbf{T}}(t))$	$\lambda_{\min}(W_{o,BT})$
(14)	0.4226	1.2924	10.04
BT	0.3369	1.6438	96.33
IRKA	0.5740	2.0202	39.88
POD	0.4373	3.5061	4.68

Fig. 12 and Table 4 enable to compare the estimator performances using the sensor locations determined based on the ROMs with those summarized in Fig. 10 and Table 3

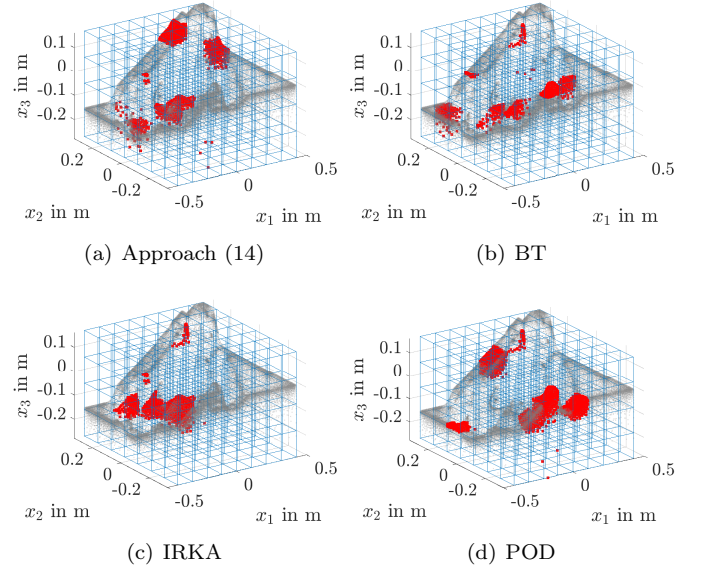


Figure 11: Selected sensor segments for (15) using different ROMs. Subfigure 11(a) is added for comparison.

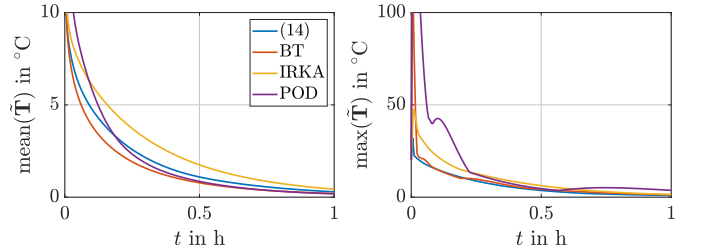


Figure 12: Comparison of their resulting estimation error for the sensor locations of Fig. 11 obtained for different ROMs.

obtained for the full order model. The mean estimation error is largest for model order reduction by the IRKA. The mean error for the POD is nearly equal to the error of the full model, but the maximum error is larger. Using MOR based on BT leads to the best estimation results. The average error in all nodes is even below the error of the full model. Table 4 also shows the function value of $\lambda_{\min}(W_{o,BT})$. Here, a higher value does not automatically lead to a smaller estimation error.

3.3.3. Variation of the number of sensors

In the previous optimizations the maximum number of sensors was chosen to be $p_{\max} = 8$. To evaluate this choice the obtained values of measure (15) using the BT-ROM with increasing p_{\max} are compared. This is depicted in Fig. 13. The value of $\lambda_{\min}(W_{o,BT})$ is rising approximately exponentially until $p_{\max} = 8$ and then changes to a linear increase. Hence, assigning $p_{\max} = 8$ seems a reasonable choice and good compromise between effort and effect as can also be seen from the estimation results in Figs. 10 and 12. It is worth noting that the maximum number of sensors p_{\max} is always equal to the actual number of

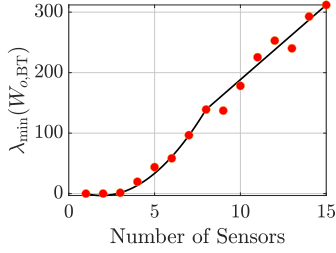


Figure 13: Measure (15) using BT-ROM for different maximum number of sensors p_{\max} .

sensors. It follows that (10b) can also be formulated as $\sum_{i=1}^p \chi_i = p_{\max}$.

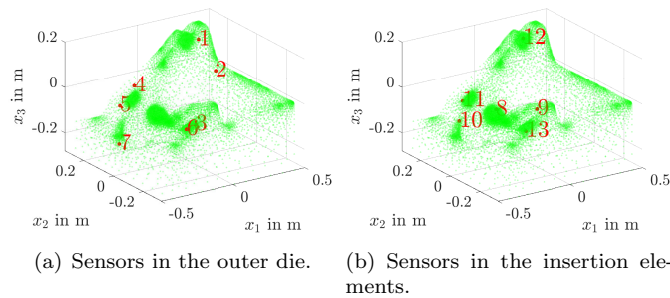


Figure 14: Placed sensors in the die: outer die and insertion elements.

Based on the presented results for optimal sensor placement the sensor configuration depicted in Fig. 14(a) is realized. The sensors are placed in the segments selected from measure (15) using BT-ROM. Herein one segment, which is located right next to an actuator, was left out as this is covered by a local thermocouple built in near the used heating cartridges. The further sensors located in the insertion elements are depicted in Fig. 14(b). The resulting output equation corresponds to (4) with $p = 13$ sensors. The numbers next to the position points define the respective index in the output vector \mathbf{y} .

4. Feedback Control Design

Knowledge of the current spatial-temporal temperature distribution is the starting point for feedback control design. For this, a linear quadratic regulator with integral part is set up combined with a Kalman filter to react efficiently to changes in the distribution resulting from disturbances or from the forming process.

4.1. Desired temperature profile

For the deep drawing tool it is in particular required to achieve a desired transient temperature profile in the six zones shown in Fig. 15. These zones include the nodes of the top surfaces of the six insertion elements.

This profile is subsequently summarized in the vector

$$\mathbf{y}_{\text{targ}} = C_{\text{targ}} \mathbf{T}, \quad t \geq 0 \quad (17)$$

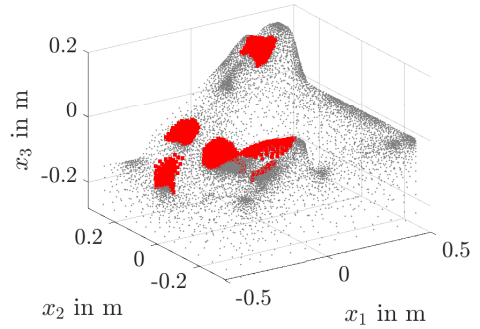


Figure 15: Die with the six red marked critical areas.

with the matrix $C_{\text{targ}} \in \mathbb{R}^{q \times n}$ extracting the mean value of the nodal temperatures from $\mathbf{T}(t)$ for each zone. The integer q is 6 as there are six zones. In steady state with the input \mathbf{u}^s and the temperature profile \mathbf{T}^s (17) can be expressed as

$$\mathbf{y}_{\text{targ}}^s = C_{\text{targ}} \mathbf{T}^s = C_{\text{targ}} (-A)^{-1} B \mathbf{u}^s.$$

Given steady state target temperatures $\mathbf{y}_{\text{targ}}^s$ the corresponding input \mathbf{u}^s hence follows by making use of the Moore–Penrose inverse, i.e.,

$$\mathbf{u}^s = (C_{\text{targ}} (-A)^{-1} B)^\dagger \mathbf{y}_{\text{targ}}^s. \quad (18)$$

Finally, (18) calculates the constant input \mathbf{u}^s required to reach the desired temperatures in the target zones $\mathbf{y}_{\text{targ}}^s$ when steady state is reached. In steady state the die including the insertion elements approaches an almost constant temperature. The actuators only counteract the heat loss via convection.

4.2. Linear–quadratic–Gaussian control

As soon as the (nearly) steady state of the temperature distribution in the die is reached, the deep drawing operations can be carried out with the die. It is expected that during a cycle the die will cool down considerably due to the cold sheet metal, which is pressed against the die by the cold punch. For this process, a controller must be designed to adjust the heating power of the actuators in such a way that the reaction to the heat loss is as fast and efficient as possible. For this purpose, a linear-quadratic (LQ) regulator is designed, which is supplemented by an integral component to counteract possible model inaccuracies. This model-based controller is amended by a Kalman filter as a state estimator. The design of the Kalman filter is described in Section 3.3. Both controller and estimator are based on the BT reduced model of dimension $r = 95$ for computability reasons.

For control design the model (16) is extended by an integral part [20]. Let $\mathbf{y}_{8:13}(t) \in \mathbb{R}^{6 \times r}$ denote the (measured) sensor values in the insertion elements according to Fig. 14(b) and let $C_{8:13}$ and $C_{r,8:13}$ denote the corresponding

submatrices of the output matrix C for the full model and for the BT-ROM. With this consider the extended system

$$\underbrace{\begin{bmatrix} E_r & 0 \\ 0 & I_6 \end{bmatrix}}_{=E_{r,\text{ex}}} \begin{bmatrix} \dot{\mathbf{T}}_r \\ \dot{\mathbf{e}}_I \end{bmatrix} = \underbrace{\begin{bmatrix} A_r & 0 \\ -C_{r,8:13} & 0 \end{bmatrix}}_{=A_{r,\text{ex}}} \begin{bmatrix} \mathbf{T}_r \\ \mathbf{e}_I \end{bmatrix} + \underbrace{\begin{bmatrix} B_r \\ 0 \end{bmatrix}}_{=B_{r,\text{ex}}} \mathbf{u} + \begin{bmatrix} 0 \\ \mathbf{y}_{8:13} \end{bmatrix} \quad (19)$$

with I_6 denoting the 6×6 identity matrix. Here, $\mathbf{e}_I = \int_0^t (\mathbf{y}_{8:13} - \hat{\mathbf{y}}_{8:13}) dt$ is the integrated estimator error of the sensors in the insertion elements. Once (19) is asymptotically stable, i.e. its rest position is reached, it follows $\mathbf{y}_{8:13} - \hat{\mathbf{y}}_{8:13} = 0$ due to $\dot{\mathbf{e}}_I = 0$. The state feedback control is then set up according to

$$\mathbf{u} = -K \begin{bmatrix} \mathbf{T}_r \\ \mathbf{e}_I \end{bmatrix} + H\mathbf{r} \quad (20a)$$

with $H \in \mathbb{R}^{m \times 6}$ a prefilter matrix and $\mathbf{r}(t) \in \mathbb{R}^6$ some reference trajectory. For the determination of K the quadratic cost functional¹

$$J = \int_0^\infty \begin{bmatrix} \mathbf{T}_r \\ \mathbf{e}_I \end{bmatrix}^T Q_c \begin{bmatrix} \mathbf{T}_r \\ \mathbf{e}_I \end{bmatrix} + \mathbf{u}^T R_c \mathbf{u}.$$

is minimized with the positive definite matrices Q_c and R_c to balance the individual contributions of the extended state $[\mathbf{T}_r(t), \mathbf{e}_I(t)]^T \in \mathbb{R}^{n_{\text{ex}}}$, $n_{\text{ex}} = r + 6$ and the input \mathbf{u} . Subsequently, diagonal matrices $Q_c \in \mathbb{R}^{n_{\text{ex}} \times n_{\text{ex}}}$ and $R_c \in \mathbb{R}^{m \times m}$ are assigned. With this

$$K = R_c^{-1} B_{r,\text{ex}}^T P. \quad (20b)$$

is obtained [30], where P solves the Riccati equation

$$0 = A_{r,\text{ex}}^T P E_{r,\text{ex}} + E_{r,\text{ex}}^T P A_{r,\text{ex}} - E_{r,\text{ex}}^T P B_{r,\text{ex}} R_c^{-1} B_{r,\text{ex}}^T P E_{r,\text{ex}} + Q_c$$

Similar to the estimator design this equation is not solvable for the full order model on a standard PC, which justifies the use of the ROM for controller design. The prefilter matrix H is in this setup used to impose that $\mathbf{y}_{\text{targ}}(t)$ defined in (17) approaches the reference trajectory $\mathbf{r}(t)$ asymptotically as $t \rightarrow \infty$. Substitution of (20a) into (19) and taking into account (17), i.e.

$$\mathbf{y}_{\text{targ}} = C_{\text{targ}} \mathbf{T} = C_{\text{targ},r} \mathbf{T}_r = C_{\text{targ},r,\text{ex}} \begin{bmatrix} \mathbf{T}_r \\ \mathbf{e}_I \end{bmatrix},$$

yields for $t \rightarrow \infty$

$$H = - \left(C_{\text{targ},r,\text{ex}} (A_{r,\text{ex}} - B_{r,\text{ex}} K)^{-1} B_{r,\text{ex}} \right)^\dagger. \quad (20c)$$

Due to the integral part in terms of $\mathbf{e}_I(t)$ an anti-windup scheme is required to address the input constraints $u_j \in [0, 1]$, $j = 1, \dots, m$. The integration is stopped whenever the constraints are violated as described in [31].

¹Note that alternatively the linear-quadratic regular can be set up to minimize the weighted difference between $\mathbf{y}_{\text{targ}}(t)$ and $\mathbf{r}(t)$.

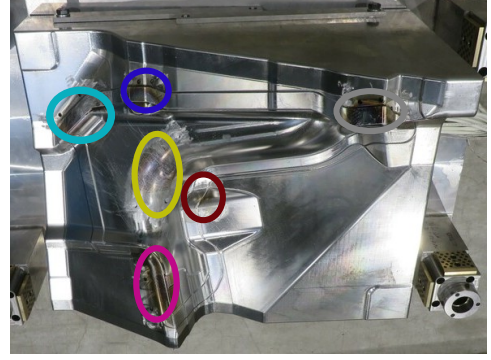


Figure 16: Top view of the experimental die. The colored ellipsoids mark the positions of the insertion elements with respect to the used colors in Fig. 2.

5. Experimental Validation

The determined model (2) and (4), the estimator design based on the BT reduced model in (16) and the chosen controller based on the BT reduced model in (19) are validated experimentally. The used experimental die is shown in Fig. 16. The sheet examined is a 1050 aluminium alloy with a thickness of 0.5 mm. For control purposes a hot runner controller (hotset HR30 from hotset) is used, which is connected to the embedded actuators and the sensors placed in the insertion elements. An USB thermocouple measurement gadget (RedLab TC from Meilhaus Electronic) reads out the temperature of the sensors placed in the outer die. Moreover, a serial connection between the COM port of an USB converter connected to a computer and the COM port of the hot runner controller via RS485 is established in the software MATLAB. Estimator and controller are implemented using MATLAB and are evaluated online on the computer with a sampling time of 1 s. The whole setup is visualised schematically in Fig. 17.

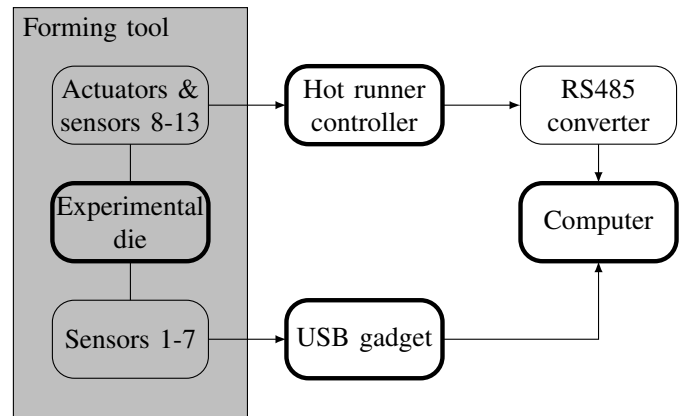


Figure 17: Experimental setup.

5.1. Estimator Validation

To analyze the performance of the Kalman filter designed based on the BT-ROM (6) eleven sensors are used

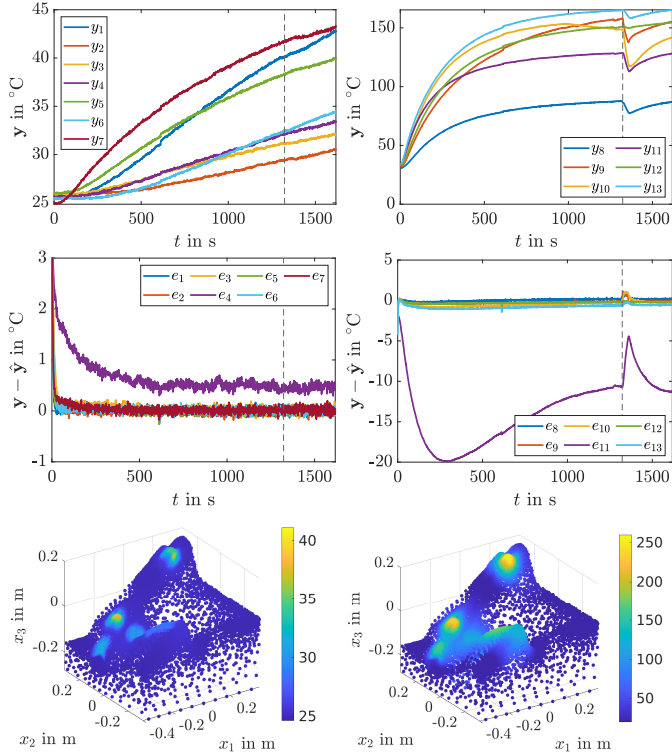


Figure 18: Temperature evolution in the die (top, left) and in the insertion elements (top, right), estimator error for sensor positions in the outer die (middle, left) and in the insertion elements (middle, right), snapshots of the estimated temperature profiles at $t = 5$ s (bottom, left) and $t = 1600$ s (bottom, right) for the scenario with constant input (21). The vertical dashed line marks the point, where the punch reaches the bottom dead point during the forming step.

for the estimator, while sensors no. 4 and 11 of Fig. 14 are used for validation purposes. This enables to compare the temperatures estimated by the filter with the temperatures measured by the sensors. From these, one is located in an insertion element while the other one is placed in the outer die. However, this setup weakens the functionality of the estimator in comparison to the one using all thirteen sensors for estimation. Two experimental scenarios are considered for the validation. The matrices Q and R are identity matrices again.

5.1.1. Heat-up with forming step

To validate the Kalman filter a scenario with constant input

$$\mathbf{u}^s = [0.2489, 0.2699, 0.2865, 0.1641, 0.2191, 0.6315]^T \quad (21)$$

is set up. This input corresponds according to (18) to a target temperature profile of $\mathbf{y}_{\text{targ}}^s = 130 \times \mathbf{1}^\circ\text{C}$ under steady state conditions inside the target zones. Due to the mapping (3) with an ambient temperature of $T_\infty = 20^\circ\text{C}$ this equals a temperature of 150°C .

Applying $\mathbf{u}(t) = \mathbf{u}^s$ the temperature in the tool rises from the initial temperature of 25°C for a period of about

1600 s. Fig. 18 shows the evolution of the sensors in the outer die (top, left) and inside the insertion elements (top, right). The respective estimator errors at all sensor locations are visualised below for those in the outer die (middle, left) and in the insertion elements (middle, right). Snapshots of the temperature profiles reconstructed by the estimator using the projection (5), i.e., $\hat{\mathbf{T}} = V\hat{\mathbf{T}}_r$, at $t = 5$ s and $t = 1600$ s are provided in the lower row. At the sensors placed inside the die the measured temperature rises nearly linear except for sensors 5 and 7, where the increase slows down a little as the steady state temperature value becomes closer. The sensors inside the insertion elements reach appropriately their steady state temperature during this scenario.

At $t = 1303$ s a forming step starts with the punch moving downwards. At $t = 1323$ s the bottom dead point is reached and is held for 30 s. At $t = 1353$ s the punch starts moving upwards to its upper dead center. Due to the contact of the die with the metal sheet, which is inserted at room temperature, a temperature drop can be observed, which is followed by a slow increase. This effect can be seen also, but to a much lower extent, in the sensors in the outer die. The evolution of the estimation errors confirms that the estimator works well. At the validation point given by sensor 4 the error reaches a negligible value of about 0.5°C . The error is higher in the insertion elements, which is confirmed by the estimator error obtained at the position of sensor 11, where a difference of up to 20°C between the Kalman filter estimation and the measurement becomes apparent that decreases successively. After the forming step this error increases again due to the contact with the metal sheet. It is worth noting that this particular difference appears next to an actuator. The difference in the outer die is much smaller, so that this error probably is just around the heater. In the whole estimator using the test sensors for estimation this error will likely be much smaller. However, no further test sensor has been placed to prove this. Despite these local differences in the quality of the estimation it can be concluded that the BT-ROM is suitable for estimator design and that the Kalman filter provides a sufficiently accurate temperature estimation in the complete die. In particular the estimator enables to reconstruct the spatial-temporal temperature profile in the tool as can be seen in terms of the snapshots shown in Fig. 18 (bottom).

5.1.2. Cool down with forming step

As a second scenario the cool down of the die is considered for $\mathbf{u} = \mathbf{0}$. Starting with temperatures of up to 500°C in the die the decay behavior shown in Fig. 19 (top row) is obtained. Forming steps are performed at times $t = 423$ s and $t = 1532$ s. In both cases the punch needs 20 s to reach the bottom dead center and stays there for 30 s. At times $t = 473$ s and $t = 1582$ s the punch starts moving upwards to its upper dead center. Due to the contact with the sheet entering the tool at approximately ambient temperature a significant cooling at the insertion elements is

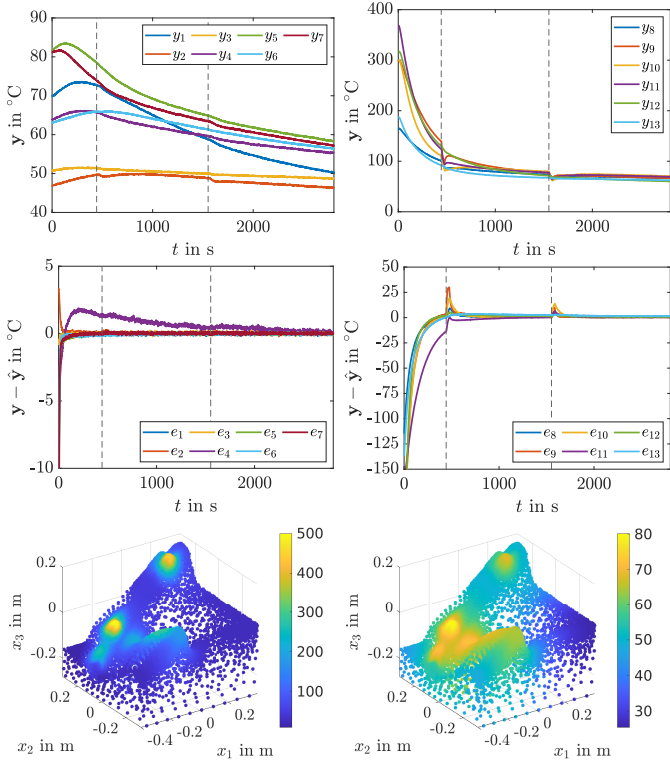


Figure 19: Temperature evolution in the die (top, left) and in the insertion elements (top, right), estimator error for sensor positions in the die (middle, left) and in the insertion elements (middle, right), snapshots of the estimated temperature profiles at $t = 100$ s (bottom, left) and $t = 2800$ s (bottom, right) for the scenario with zero input $\mathbf{u} = \mathbf{0}$. The vertical dashed lines mark the points, where the punch reaches the bottom dead point during the forming steps.

initiated. The estimator errors shown in Fig. 19 (middle row) converge to zero in both the outer die (see validation sensor 4) and the insertion elements (see validation sensor 11). During the forming steps a short rise can be seen due to the changed contact situation. The estimated spatial-temporal temperature profiles shortly after the beginning and at the end of the cool down with forming steps are depicted in Fig. 19 (bottom row).

5.2. Controller Validation

The controller presented in Section 4.2 is experimentally validated. Starting with a non-steady state profile the state feedback (20) is evaluated using the estimated states obtained from the Kalman filter (19). While the latter is again tuned with the identity matrices Q and R , the LQ controller is tuned with an identity matrix Q_c and a diagonal matrix R_c with

$$\text{diag } R_c = [1.8, 1.45, 1.2, 1.05, 1.4, 1.25]^T 10^6.$$

The reference trajectory is assigned constant with

$$\mathbf{r}(t) = [130, 130, 130, 130, 130, 130]^T \text{ } ^\circ\text{C}$$

to reach the demanded temperature of $150 \text{ } ^\circ\text{C}$ in the target zones for $T_\infty = 20 \text{ } ^\circ\text{C}$. The considered scenario includes

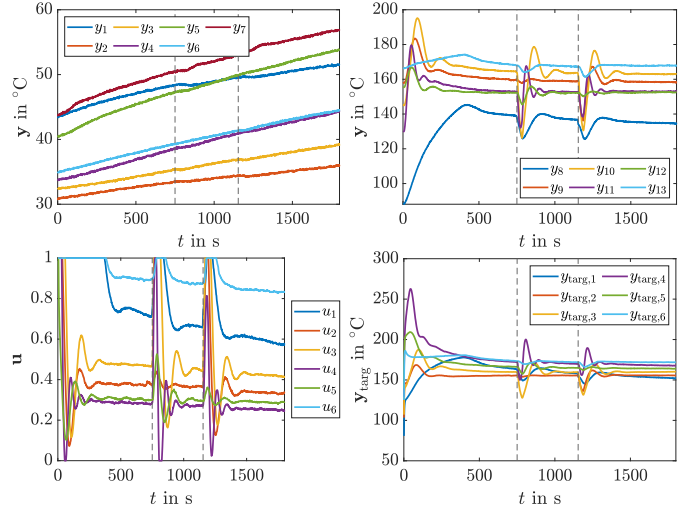


Figure 20: Temperature evolution in the outer die (top, left) and in the insertion elements (top, right), the applied control inputs (bottom, left) and the target output (bottom, right) for the LQ-regulator with integral part. The vertical dashed lines mark the points, where the punch reaches the bottom dead point during the forming steps.

two forming steps, which are performed at times $t = 730$ s and $t = 1134$ s. In both cases the punch again needs 20 s to reach the bottom dead center and stays there for 30 s. At times $t = 780$ s and $t = 1184$ s the punch starts moving upwards to its upper dead center.

The obtained results are summarized in Fig. 20. The temperature at the sensors in the die rises approximately linearly, while the sensors in the insertion elements all reach a nearly constant temperature after about $t = 500$ s except during forming, see Fig. 20 (top row). Starting when the die is at the bottom dead center during the forming steps, it takes about 120 s until the sensors in the insertion elements reach the temperature level before forming. This is a significant improvement towards the heat-up case in Fig. 18, where it takes about 300 s. The two diagrams in the bottom row show the elements of the input vector \mathbf{u} and the target output \mathbf{y}_{targ} . The input is nearly constant after about 500 s but is rising to maximum power when the forming operations take place. The values are nearly proportional to the input (21), which guarantees the desired temperature profile in the steady state. As the steady state is not completely reached the inputs are higher by a factor of about 1.5. The reached target outputs are slightly larger than the desired $150 \text{ } ^\circ\text{C}$. This might be due to the rising input power during the forming steps. However, as the target temperatures almost never fall below the reference the formability of the metal during the forming process is guaranteed.

6. Conclusions and outlook

In this paper a temperature control strategy is developed for a deep drawing tool with embedded actuation

and sensing devices to reduce wrinkles and cracks by increasing the formability of the metal sheet to be formed.

Based on a continuum model of the spatial-temporal temperature distribution in the die a finite element approximation is deduced. By systematically making use of model order reduction techniques the large-scale approximation is projected onto a suitable subspace of significantly smaller dimension to obtain a model setup that can be used for control and estimator design. A parameter identification is performed based on experimental data to determine the heating power of the actuators and the heat transfer coefficients. Optimal sensor placement is performed using a suitable optimization strategy involving the determined reduced order models. The sensor locations obtained from different cost functionals in terms of the observability Gramian are compared based by setting up a Kalman filter to evaluate the resulting estimation performance. This serves as basis for the targeted intervention by built-in actuators. The best result was achieved by maximizing the smallest eigenvalue of the reduced order model obtained by balanced truncation. The estimator-based feedback control is set up as a linear-quadratic regulator extended by an integral part to react efficiently to disturbances. For the experimental validation the system design in terms of optimal sensor placement is realized in an experimental forming tool and the developed control strategy involving the estimator based on a reduced order model is implemented under real-time requirements.

The obtained experimental results clearly support the applicability of this consistent design process and confirm the control and estimation performance to maintain desired prescribed local target temperatures during forming. It is also shown that in a scenario with multiple consecutive forming steps the demanded temperature can be kept at the demanded level.

Possible improvements of the presented approach in future research are summarized subsequently. Within the project only the local heating of one half of the tool, the bottom die, is considered. It is also possible to think of a local heating of the punch of the tool. Another aspect can be the heating of the blank before the forming process. This could also improve the formability. Moreover, the placement of another sensor could improve the validation of the estimator. This enables the possibility to proof the functionality of the Kalman filter using all placed sensors. Furthermore, another optimization algorithm can be used to compare the results of the optimal sensor placement problem. Here, a simple greedy algorithm as discussed in [13] could be considered. As already pointed out the number of sensors can be fixed to reduce the complexity of the sensor placement problem. It is important to test this framework in a production line with higher stroke rate, as the maximum number of forming operations per time interval at which the actuator and the controller can reliably operate has not been evaluated in this work. However, a significant improvement has been achieved to maintain the operating condition by the proposed temperature control.

Acknowledgement

The financial support by the Bundesministerium für Wirtschaft und Klimaschutz (German Federal Ministry for economic affairs and climate action (BMWK)) by the Zentrales Innovationsprogramm Mittelstand (ZIM) in the project ref. ZF4558805RU8 is gratefully acknowledged.

References

- [1] Z. Gronostajski, Z. Pater, L. Madej, A. Gontarz, L. Lisiecki, A. Łukaszek-Solek, J. Luksza, S. Mróz, Z. Muskalski, W. Muzykiewicz, et al., Recent development trends in metal forming, *Archives of Civil and Mechanical Engineering* 19 (3) (2019) 898–941.
- [2] J. Jeswiet, M. Geiger, U. Engel, M. Kleiner, M. Schikorra, J. Dufflou, R. Neugebauer, P. Bariani, S. Bruschi, Metal forming progress since 2000, *CIRP Journal of Manufacturing Science and Technology* 1 (1) (2008) 2–17.
- [3] V. Boljanovic, Deep drawing, in: *Sheet Metal Forming Processes and Die Design*, Industrial Press, 2004, Ch. 5, pp. 69–84.
- [4] Schuler GmbH, Basic principles of metal forming, in: *Metal Forming Handbook*, Springer Berlin Heidelberg, Berlin, Heidelberg, 1998, pp. 5–32.
- [5] S. Toros, F. Ozturk, I. Kacar, Review of warm forming of aluminum–magnesium alloys, *Journal of Materials Processing Technology* 207 (1-3) (2008) 1–12.
- [6] O. Zienkiewicz, R. Taylor, J. Zhu, *Variational forms and finite element approximation: 1-d problems*, in: *The Finite Element Method: its Basis and Fundamentals*, 7th Edition, Butterworth-Heinemann, Oxford, 2013, Ch. 4, pp. 93–113.
- [7] P. Benner, S. Gugercin, K. Willcox, A Survey of Projection-Based Model Reduction Methods for Parametric Dynamical Systems, *SIAM Review* 57 (2015) 483–531.
- [8] T. Böhm, T. Meurer, Trajectory planning and tracking control for the temperature distribution in a deep drawing tool, *Control Engineering Practice* 64 (2017) 127 – 139.
- [9] P. Benner, R. Herzog, N. Lang, I. Riedel, J. Saak, Comparison of model order reduction methods for optimal sensor placement for thermo-elastic models, *Engineering Optimization* 51 (2018) 1–19.
- [10] T. Nestorović, M. Trajkov, Optimal actuator and sensor placement based on balanced reduced models, *Mechanical Systems and Signal Processing* 36 (2013) 271–289.
- [11] K. Manohar, J. N. Kutz, S. L. Brunton, Optimal sensor and actuator selection using balanced model reduction, *IEEE Transactions on Automatic Control* 67 (4) (2022) 2108–2115.
- [12] M. Serpas, G. Hackebeil, C. Laird, J. Hahn, Sensor location for nonlinear dynamic systems via observability analysis and MAX-DET optimization, *Computers and Chemical Engineering* 48 (2013) 105 – 112.
- [13] T. H. Summers, F. L. Cortesi, J. Lygeros, On Submodularity and Controllability in Complex Dynamical Networks, *IEEE Transactions on Control of Network Systems* 3 (1) (2016) 91–101.
- [14] A. C. Antoulas, *Approximation of Large-Scale Dynamical Systems*, Society for Industrial and Applied Mathematics, 2005.
- [15] J. Andrej, T. Meurer, Flatness-based constrained optimal control of reaction-diffusion systems, in: *2018 Annual American Control Conference (ACC)*, 2018, pp. 2539–2544.
- [16] T. Meurer, J. Andrej, Flatness-based model predictive control of linear diffusion-convection-reaction processes, in: *2018 IEEE Conference on Decision and Control (CDC)*, 2018, pp. 527–532.
- [17] M. Fliess, J. Lévine, P. Martin, P. Rouchon, Flatness and defect of non-linear systems: introductory theory and examples, *International Journal of Control* 61 (6) (1995) 1327–1361.
- [18] P. Benner, J. Saak, Linear-quadratic regulator design for optimal cooling of steel profiles, *Tech. Rep. SFB393/05-05*, Sonderforschungsbereich 393 it Parallele Numerische Simulation

für Physik und Kontinuumsmechanik, TU Chemnitz, D-09107 Chemnitz (Germany) (2005).

- [19] J. Fisher, R. Bhattacharya, Linear quadratic regulation of systems with stochastic parameter uncertainties, *Automatica* 45 (12) (2009) 2831–2841.
- [20] P. C. Young, J. C. Willems, An approach to the linear multivariable servomechanism problem, *International Journal of Control* 15 (5) (1972) 961–979.
- [21] F. Rathgeber, D. A. Ham, L. Mitchell, M. Lange, F. Luporini, A. T. T. McRae, G.-T. Bercea, G. R. Markall, P. H. J. Kelly, Firedrake: automating the finite element method by composing abstractions, *ACM Trans. Math. Softw.* 43 (3) (2016) 24:1–24:27. arXiv:1501.01809.
- [22] S. L. Brunton, J. N. Kutz, Balanced models for control, in: *Data-Driven Science and Engineering: Machine Learning, Dynamical Systems, and Control*, Cambridge University Press, 2019, Ch. 9, pp. 321–344.
- [23] P. Benner, P. Kürschner, J. Saak, An improved numerical method for balanced truncation for symmetric second-order systems, *Mathematical and Computer Modelling of Dynamical Systems* 19 (6) (2013) 593–615.
- [24] J. Saak, M. Köhler, P. Benner, M-M.E.S.S.-2.0.1 – the matrix equations sparse solvers library, DOI:10.5281/zenodo.3606345, see also: www.mpi-magdeburg.mpg.de/projects/mess (Feb. 2020).
- [25] S. Gugercin, A. Antoulas, C. Beattie, H2 Model Reduction for Large-Scale Linear Dynamical Systems, *SIAM J. Matrix Anal. Appl.* 30 (2) (2008) 609–638.
- [26] A. Castagnotto, M. Cruz Varona, L. Jeschek, B. Lohmann, sss & sssmor: Analysis and reduction of large-scale dynamic systems in matlab, *at-Automatisierungstechnik* 65 (2) (Feb 2017).
- [27] K. Kunisch, S. Volkwein, Galerkin proper orthogonal decomposition methods for parabolic problems, *Numerische Mathematik* 90 (1) (2001) 117–148.
- [28] S. Kakac, Y. Yener, A. Pramuanjaroenkij, *Convective heat transfer*, CRC press, 2013.
- [29] M. Wrobel, T. Meurer, Optimal sensor placement for temperature control in a deep drawing tool, *IFAC-PapersOnLine* 54 (11) (2021) 91–96, 6th IFAC Workshop on Mining, Mineral and Metal Processing MMM 2021.
- [30] A. Gelb, *Applied Optimal Estimation*, MIT Press, Cambridge, 1974.
- [31] P. Hippe, Prevention of controller windup, in: *Windup in Control: Its Effects and Their Prevention*, Springer London, London, 2006, Ch. 2, pp. 21–57.